# Characterization of Crater Morphometry on the Moon and Mercury from Altimetry Observations

by

Matthieu Jean Talpe

B.S., Earth, Atmospheric and Planetary Sciences
Massachusetts Institute of Technology, 2011

Submitted to the Department of Earth, Atmospheric and Planetary Sciences
in partial fulfillment of the requirements for the degree of

Master of Science in Planetary Sciences

at the

MASSACHUSETTS INSTITUTE OF TECHNOLOGY

June 2012





Author .....
Department of Earth, Atmospheric and Planetary Sciences
May 11, 2012

Certified by .....
Maria T. Zuber
E. A. Griswold Professor of Geophysics
Thesis Supervisor

Accepted by .....
Robert D. van der Hilst
Schlumberger Professor of Geosciences
Head, Department of Earth, Atmospheric and Planetary Sciences

# Characterization of Crater Morphometry on the Moon and Mercury from Altimetry Observations

by

Matthieu Jean Talpe

Submitted to the Department of Earth, Atmospheric and Planetary Sciences
on May 11, 2012, in partial fulfillment of the
requirements for the degree of
Master of Science in Planetary Sciences

## Abstract

Recently acquired altimetry data from laser altimeters are used to assess the morphometry of impact craters. Data acquired by the Mercury Laser Altimeter on the MESSENGER spacecraft are used to measure the depths and diameters of 537 craters at the high northern latitudes on Mercury, including 42 polar-deposit-hosting craters (PDCs) which host material that is bright to earth-based radar observations. A comparative analysis suggests that the radar-bright material forms a thin ($< 20$ m) layer emplaced preferentially in comparatively young craters, contradicting an earlier morphometric study that indicated that PDCs contained a thick layer of water ice and dust. Topographic datasets from the lunar surface, collected by the Lunar Orbiter Laser Altimeter onboard the LRO spacecraft, are also used to evaluate the morphometry of 1,356 lunar craters. We study the morphologic change between the simple and complex crater regime, a manifestation of the transition between gravity-dominated and strength-dominated impact-forming processes, on the Moon and Mercury. The Moons transition diameter is near 16 km, in line with previous studies, while Mercurys is near 8 km, 2 km smaller than previously determined. The onset of gravity-dominated mechanisms scales inversely with gravity, which explains why Mercurys transition diameter is approximately half of the Moons.

Thesis Supervisor: Maria T. Zuber
Title: E. A. Griswold Professor of Geophysics

# Acknowledgments

First and foremost I would like to thank Professor Maria Zuber for her guidance and support. Like most of my peers, I found the MIT undergraduate experience extraordinarily stimulating but also overwhelming at times. Staying on for a fifth-year Master's allowed me to piece together some of the knowledge acquired hastly as an undergrad by adding a few months of perspective. In this ever-so-short ten-month experience, my understanding and appreciation of both the scientific method and planetary sciences have grown enormously. As such, I am profoundly indebted to Maria for keeping me onboard and funding this fifth-year Master's program.

I am thankful to have participated in an incredibly enriching seminar at the Barringer Meteorite Crater. For a full week fifteen students and I trekked along the rims, down and up the walls, and on the floor of the world's best preserved crater with Dr. David Kring of the Lunar and Planetary Institute sharing much of his knowledge of the "geologic reality" of impact cratering. I am grateful to have been part of several enlightening and inspiring trips–the GRAIL launch, the MESSENGER Science Team meeting, AGU and LPSC. I am also indebted to Professor Taylor Perron for taking the time to answer some of my questions, Professor Rick Binzel for a three-hour conversation 4 years ago that motivated me to matriculate as a Course XII student, and Professor Ben Weiss for his great classes and contagious enthusiasm.

Thanks are extended to friends in the department–Frank, Anton, Michael, Peter, Alex, Yodit, ZhenLiang, Katie P., Paul, Di, and many others–for their companionship and in particular to Anton for being a reliable source of feedback (always much appreciated). Finally, I owe many thanks to friends on the MIT cycling and triathlon teams–Benoit, Adam, Katie Q., and more–for providing me with an excuse to lead a decently healthy lifestyle and enjoy the thrill of racing, as well as my family on both sides of the Atlantic and in Boston for their resolute support throughout the year.

I dedicate this thesis to my deceased grand-father, Walter Talpe, a man of few words who led by example and was appreciated by many.

# Contents

# List of Figures

# List of Tables

# Chapter 1

# Introduction

The recent revival of robotic exploration of the solar system is greatly improving our understanding of the formation and evolution of the solar system. Modern remote-sensing instruments have yielded an unprecedented amount of high-resolution data of a variety of types. The data of interest in this thesis are topography and the planetary bodies studied are the the Moon and Mercury, the two "dead" airless bodies of the inner solar system.

The topographic datasets have been generated from data acquired by altimeters onboard the Lunar Reconnaissance Orbit (LRO) and the MErcury Surface, Space ENvironment, GEochemistry and Ranging (MESSENGER) spacecrafts. LRO has been studying the lunar environment since 2009 and carries seven instruments as part of its scientific payload, including a laser altimeter (LOLA) and cameras (LROC). MESSENGER inserted around Mercury on 18 March 2011 after a seven-year journey through the inner solar system and its payload also includes a laser altimeter (MLA) and cameras (MDIS).

Over the past ten months I have examined this altimetry data to evaluate the shape of impact craters, the most ubiquitous surface features of the Moon and Mercury. Specifically, I assess the morphometry of craters with diameter size ranging between 1 and 250 km, with the large majority of the craters between 5 and 50 km in diameter.

When bolides collide with a planetary surface, crustal material is melted, vapor-

ized, and excavated as the kinetic energy of the impactor is partitioned at the site of the impact. By acting as natural drill holes, craters provide insight on sub-surface geology. Furthermore, the surfaces of the Moon and Mercury remain essentially intact over billions of years because many of the rapid crater-removal mechanisms operating on Earth (tectonic recycling, volcanic resurfacing, atmospheric and aqueous erosion, etc.) are absent or weak. Craters therefore provide a unique record of the geologic evolution of the Moon and Mercury.

*"Larger samples [of crater morphologies] are feasible only if the process of counting and classifying craters is totally automated with a direct computer linkage. One's sanity can survive only so much crater counting!"*
George E. McGill, 1973, in *Morphology of Lunar Craters: A Test of Lunar Erosional Models.*

# Chapter 2

# Polar Deposits In Mercury's North Polar Region

## 2.1 Background

Earth-based radar imaging of Mercury dating back two decades revealed that a number of areas near both poles of the planet display high radar reflectivity at 3.5-cm [1, 2] and 12.6-cm wavelengths [3, 4, 5] (Figure 1). Images acquired from Mariner 10 flybys in 1974 and 1975 indicated that the locations of many of those radar-bright features are correlated with the interiors of impact craters [6, 7].

Several hypotheses have been put forth to explain the source of the radar-bright deposits: volcanic outgassing of volatiles [1], production of sodium and water vapor from the chemical sputtering of surface rocks driven by magnetospheric protons [8], deposition of exogenous volatiles from cometary and meteoroid impacts [9, 10], high local concentrations of sulfides mixed in the regolith [11], and decreased dielectric loss in silicate material at low polar temperatures [12]. In addition, modeling of the thermal environment at the poles indicates that some forms of volatiles (e.g., water ice) could be stable in permanently shadowed regions of polar craters for timescales

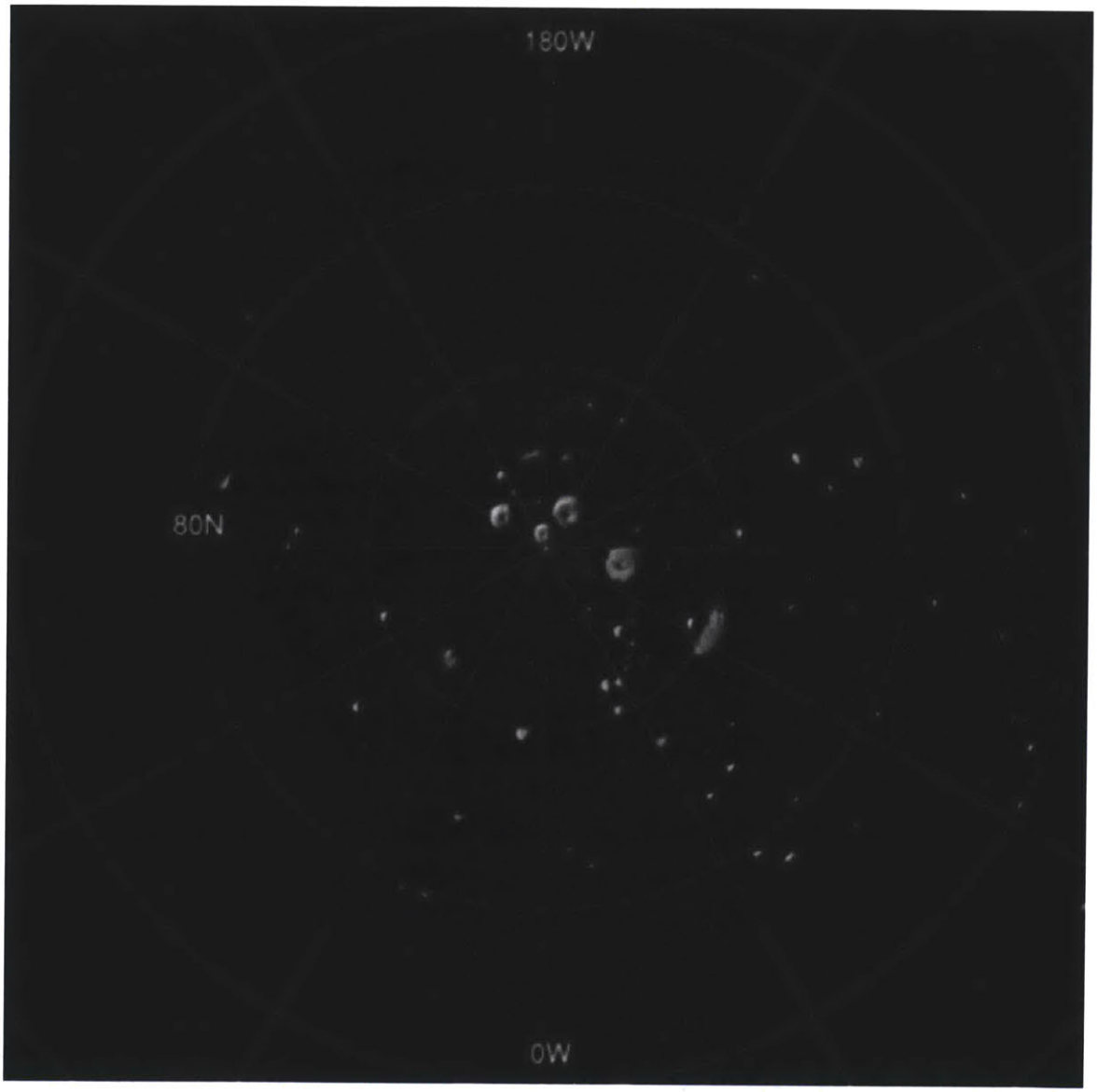


Figure 2-1: Stereographic projection of areas of high radar reflectivity in Mercurys north polar region. From Harmon et al. [7].

exceeding 1 G.y. [13, 14, 15].

The scientific payload of the MErcury Surface, Space ENvironment, GEochemistry, and Ranging (MESSENGER) spacecraft has made a number of observations relevant to the nature of radar-bright polar deposits since MESSENGER inserted into orbit about Mercury on 18 March 2011. These observations include the discovery from MESSENGER's X-Ray Spectrometer (XRS) that Mercury has a high overall surface abundance of sulfur (up to 4 wt%) [16], the measurement of generally low reflectivity of radar-bright material at the 1064-nm wavelength of MESSENGER's Mercury Laser Altimeter (MLA) [17], and the demonstration that radar-bright material polar deposits coincide with areas of permanent shadow in images acquired by MESSENGER's Mercury Dual Imaging System (MDIS) [18, 19]. Recent updates to thermal models of impact craters at high latitudes have also explored the range of stability of impact-delivered organic compounds as well as water ice in polar cold traps [20, 21].

In this paper we use observations from MESSENGER's MLA instrument [22] to address the following two questions. What does a systematic survey of crater morphometry indicate about the north polar region of Mercury? Does the radar-bright material affect the morphology of these polar-deposit-hosting craters (PDCs)?

In an earlier study, the shape of 170 craters distributed at both poles and some of the equatorial quadrangles were measured and compared on a regional basis [23]. That study was motivated by a similar analysis on Martian craters, which showed that subsurface ice accelerates topographic relaxation, resulting in smaller crater depths at a given crater diameter at higher latitudes [24, 25]. However, no such regional variation in the relation between crater depth and diameter was detected on Mercury.

A more recent study of the morphometry of 12 PDCs located near Mercury's north pole yielded the conclusion that the mean ratio of crater depth to rim-crest diameter for the PDCs is two-thirds that of the mean ratio for a comparable population of

neighboring craters lacking such deposits [26]. One explanation put forward to explain this shoaling is that the floors of the PDCs contain a thick (hundreds of meters) layer of volatiles mixed with non-volatile material such as dust delivered by the impacts of volatile-rich comets or asteroids [26].

Both the studies of [23] and of [26] involved the application of photoclinometric techniques to Mariner 10 images. In those methods, measurements of shadow lengths and knowledge of ephemerides and spacecraft attitude are combined to estimate variations in topographic elevation. In contrast, we use here the geodetically controlled altimetry data acquired by the MLA to assess the geometric properties of craters and avoid the uncertainties of photoclinometric techniques.

## 2.2 Methods

### 2.2.1 From altimetry to topography

The MLA is a laser rangefinder that determines topography from pulse-edge timing [22]. The MLA transmits a 1064-nm laser pulse at 8 Hz, illuminating surface areas between 15 m and 100 m in diameter and spaced approximately 400 m apart along the spacecraft ground track [27]. The radial precision of individual measurements is better than 1 m, and the accuracy with respect to Mercury's center of mass is better than 20 m [Smith et al., 2012]. MESSENGER's eccentric orbit during the primary mapping mission (200-km periapsis at 60°N73°N and 15,200-km apoapsis in a 12-h period) and MLA instrument specifications (off-nadir observations are limited to slant angles of less than 40° from the vertical and 1,000-km range) constrain altimetry coverage northward of 15°S.

The range of the altimeter from Mercury's surface is computed from the time-of-flight of each laser pulse and then converted into an elevation relative to a reference sphere of radius 2440 km from known spacecraft attitude and an orbital position

determined from spacecraft radio tracking [28]. As of early March 2012, MLA had collected more than 6.2 million altimetry shots and produced a comprehensive topographic map of Mercury's northern hemisphere [27].

### 2.2.2 Crater selection

For this study we used over 4.25 million altimetry points from MLA's channel 0, the instrument channel with highest signal-to-noise ratio. The observations were acquired from the time of MESSENGER orbit insertion on 18 March 2011 until mid-February 2012, when the MLA was turned off to manage the thermal stresses incurred during a high-temperature phase of the orbit.

We also used images collected from MESSENGER's MDIS cameras [29] to complement altimetry data in selecting craters. The MDIS consists of a multi-spectral wide-angle camera and a monochrome narrow-angle camera and has generated a global mosaic of images at an average spatial resolution of 250 m per pixel that covers more than 90% of Mercury's surface [30].

The altimetry coverage corresponds to the ground tracks of MLA profiles obtained during nearly 450 orbits. The spacing between each ground track is smallest where the tracks intersect near 82.5°N (the orbit inclination) and largest at lower latitudes. Hence, many craters with diameters smaller than the ground track spacing at the lower latitudes are not covered by this altimetry dataset. This latitudinal variation in cross-track coverage introduces a bias in the craters measured in this study; craters with the smallest diameters sufficiently well sampled by altimetry are mostly located at higher latitudes. Furthermore, the number of points in MLA's channel 0 decreases in areas with high topographic roughness, e.g., the rims and floors of small craters. The minimum coverage required for a crater to be selected in this study is one crater-centric track (i.e., passing sufficiently close to a crater center to include a representative portion of the crater floor and rims) with good sampling of altime-

try on the rims and on the crater floor. The assessment of adequacy of sampling is somewhat qualitative and depends on the topographic coverage; some craters are well profiled by less than 20 MLA shots that sample the rims and floor better than at other craters for which more than 50 shots sample only the rims or unrepresentative portions of the crater floor. Comparison of MDIS images to MLA profile location provides a further basis for the assessment of MLA coverage reliability.

In addition to coverage constraints, we considered a crater's morphologic state. Craters with obliterated rims, infilled floors, embayed features, and/or superposed topographic features were not selected for further analysis on the grounds that their topography is unrepresentative of craters unmodified by such processes.

### 2.2.3 Morphometric measurements

We used the geodetically controlled altimetry data provided by MLA to evaluate two standard geometric measures of craters, rim-crest diameter $D$ and crater depth $d$. We also assessed the surface roughness of the crater floors over a range of horizontal baselines and evaluated the slopes of poleward- and equator-facing crater walls.

#### Crater geometry

The rim-crest diameter $D$ was found by fitting a circle to the crater rims by least squares (Figure 2). The rim positions were defined as the two maximum elevations on either side of the crater floor for most crater-centric altimetry profiles. The least squares fit yields a crater center and a diameter with an associated standard deviation.

The crater depth $d$ is defined as the difference between the rim elevation and the floor depth (Figure 3). The rim elevation is taken to be the mean of the highest half of the rim altimetry points, on the grounds that topography-reducing mechanisms are more common than topography-augmenting mechanisms at crater walls. Topography-reducing mechanisms at crater walls are driven by the inherent diffusion of landscapes

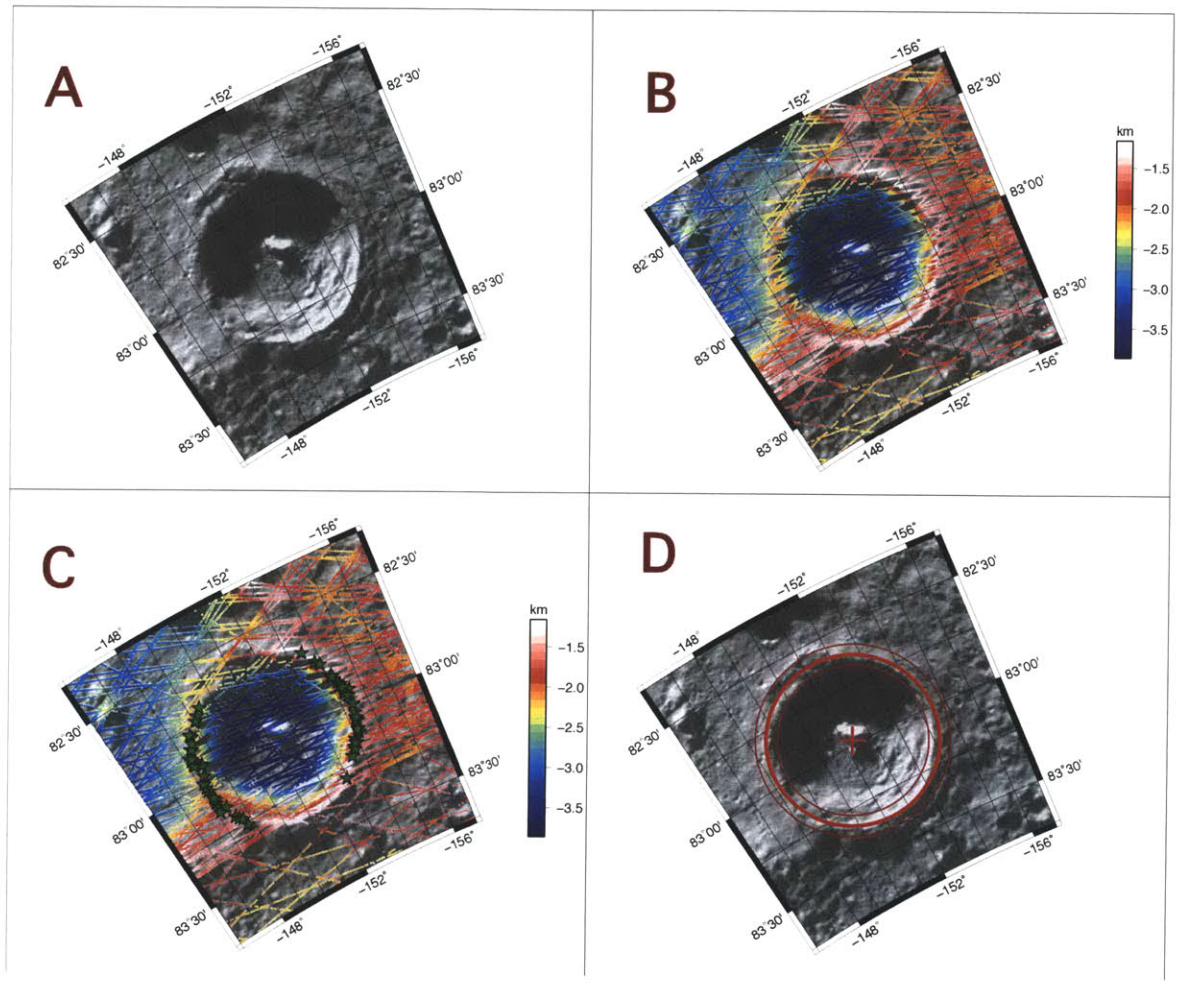


Figure 2-2: Illustration of the method used to determine crater diameter. (a) Image extracted from a global mosaic of MDIS images of an unnamed, complex 33-km-diameter crater centered at 83°N, 208°E. This crater does not host polar deposits. (b) Plan view with overlaid MLA tracks, color-coded by elevation. (c) The crater rim positions, designated by the green stars, are determined from the highest elevations in the vicinity of the imaged rim. (d) The rim-crest diameter is computed from a least squares fit of a circle (thick red line) to rim locations. The crater center position is indicated the plus sign, and one standard deviations on the crater diameter are denoted the two thin red circles.

as well as stochastic processes such as the alteration or obliteration of existing rims by subsequent impacts. The altimetry points used in assigning the depth of a floor were selected manually to avoid the bias of superposed craters. The high topographic variability of the rim (due in part for the crater in Figures 2 and 3 because it overlaps the rim of a larger crater) translates to a large standard deviation for the rim elevation measurements.

Inspection of equivalent MDIS coverage was used to corroborate the MLA-derived measurements and to discard craters with uncharacteristic morphologies or insufficient MLA sampling. In the latter category, for instance, are cases for which the best fit circle doesn't follow the physical crater diameter and profiles that sample only the lower crater walls rather than the crater floor.

### Crater floor roughness

We used a technique developed by *Kreslavsky and Head* [31] to assess the roughness of the Martian surface. This technique has also been applied to distinguishing terrain types on Mercury from MLA observations [32] and on the Moon from observations by the Lunar Orbiter Laser Altimeter [33].

The roughness at a point on the crater floor R is defined as the absolute value of the differential slope s,

$$R = \arctan(s) \tag{2.1}$$

where the differential slope s is defined as

$$s = |s_L - s_{2L}| \tag{2.2}$$

and where $s_L$ and $s_{2L}$ are the slopes of baselines of length $L$ and $2L$, respectively, centered at the point of interest. The slope of each baseline is defined as the slope

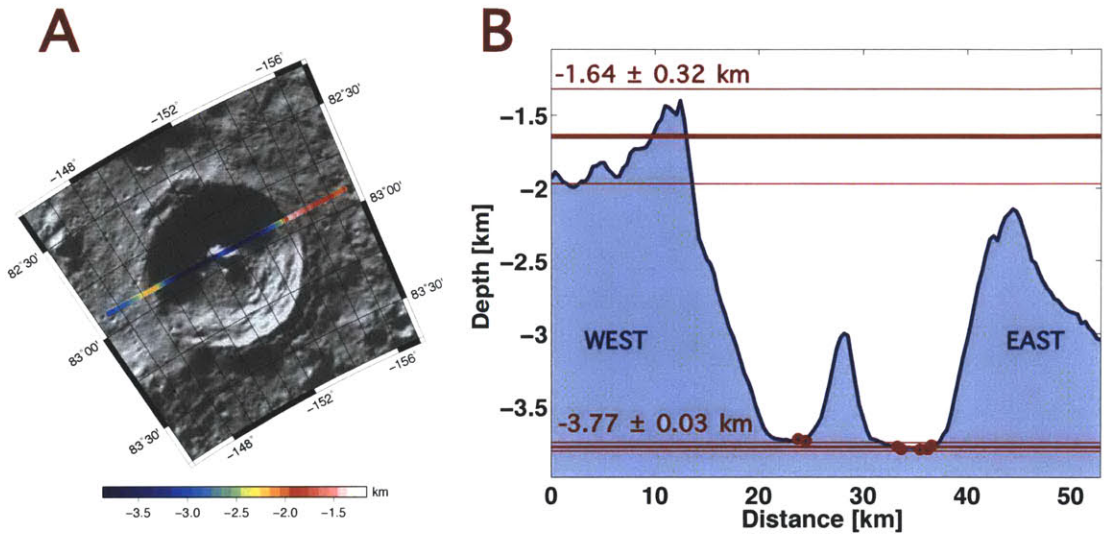


Figure 2-3: Illustration of the method used to determine crater depth. (a) Plan view of the crater in Figure 2 with a near-center-crossing MLA profile overlaid. (b) Topographic cross-section along the selected MLA profile. Thick red lines denote the measured elevations of the rim and floor and one standard deviations are denoted by the thin red lines.

of the line connecting the two baseline endpoints (Figure 4). For this study, we explored slopes for which $L$ was 0.8, 3.2, or 5.6 km (i.e., $2L$ was 1.6, 6.4, or 11.2 km). Subtracting the longer baseline slope from the shorter baseline slope in the expression for differential slope in equation 2.2 tends to remove the influence of large-scale topographic trends, and calculating the differential slope over several length scales permits an exploration of roughness versus horizontal wavelength. The absolute value operator is applied to the slope difference in equation 2.2 because a negative differential slope and a positive equivalent contribute similar information to the characterization and comparison of surface roughness on crater floors. We have taken the roughness for a particular crater floor to be the median values of all the differential slopes for that floor.

### Crater wall angle

We parameterized the slope of crater walls as a quasi-linear rise in elevation between the base of the wall and the crater rims (Figure 5). Areas of high roughness or surface curvature, such as the rim crests and the transition between the flat crater floor and the wall, were not included in the determination of the crater wall angle. The angle $\alpha$ with respect to the horizontal was defined from the rise in elevation of the wall and the horizontal distance over which that rise can be traced.

We distinguished between north-facing and south-facing walls. *Chabot et al.* [18] and *Neumann et al.* [17] have noted that radar-bright feature is primarily found only on or near southernmost, north-facing crater walls in most craters at high northern latitudes. Therefore, the angles of the northern and southern walls of PDCs were measured separately in order to investigate the possible influence of radar-bright material on wall slopes.

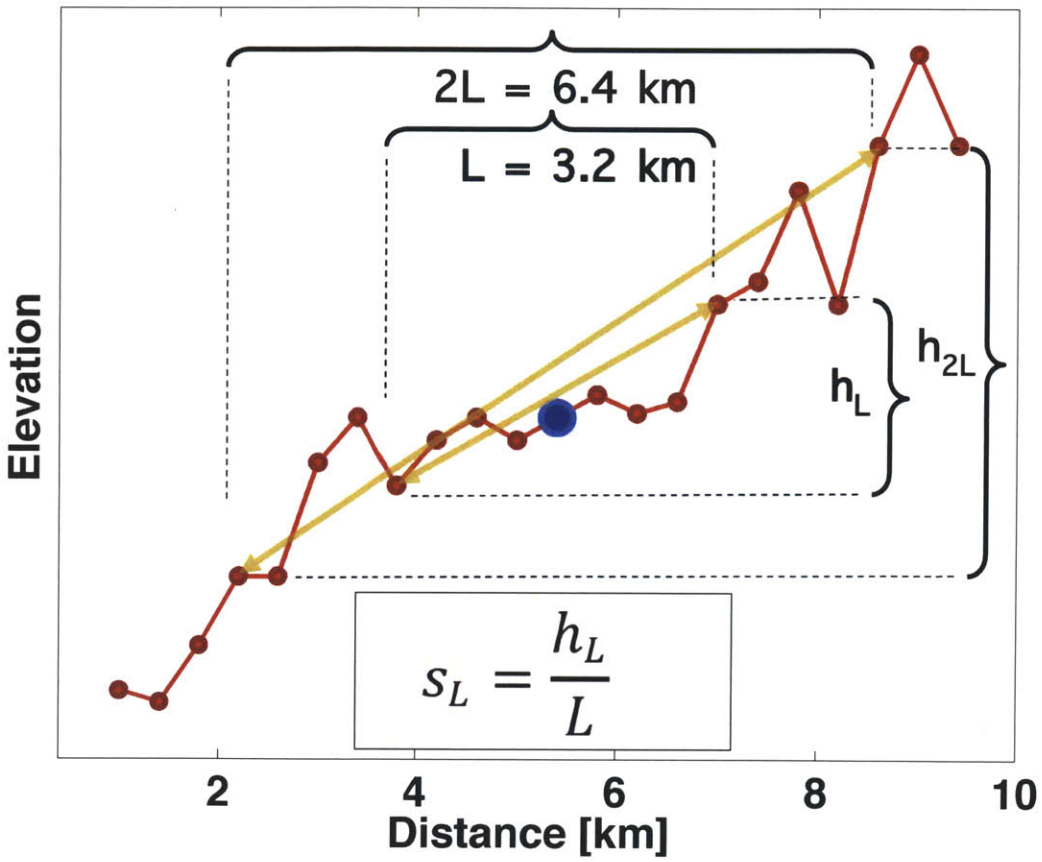


Figure 2-4: Illustration of the measurement of slope $s_L$ over a baseline of length $L = 3.2$ km at a given point (blue circle) along a topographic profile for which successive observation points (red circles) are separated by 400 m.

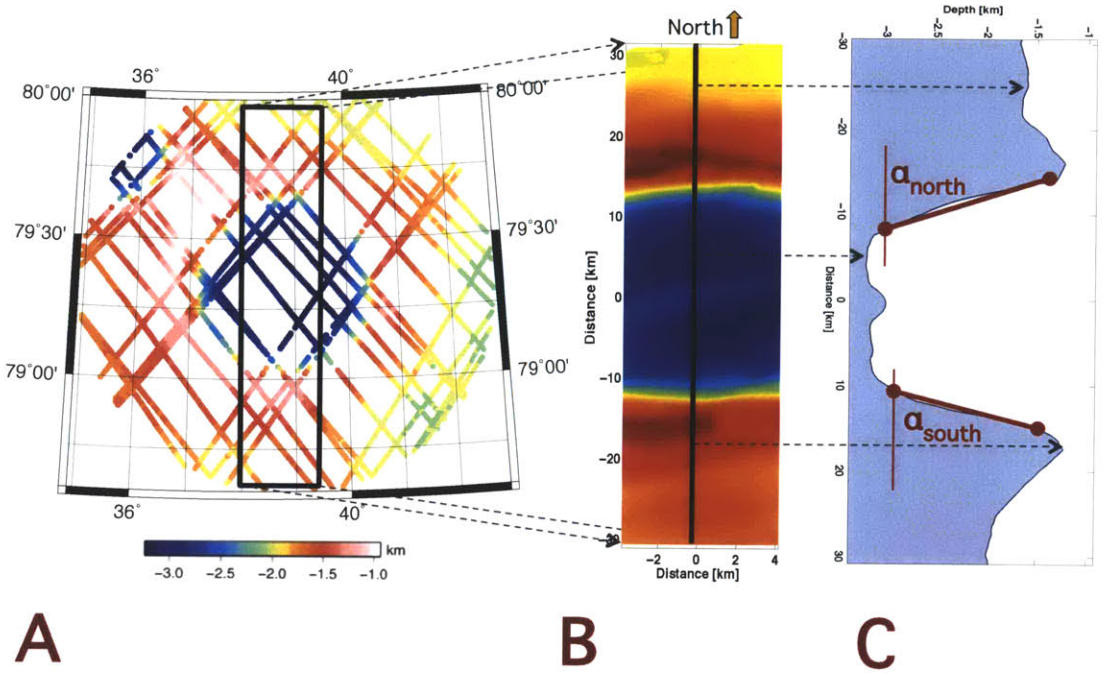


Figure 2-5: Illustration of the measurement of crater wall slope. (a) MLA coverage of an unnamed polar-deposit-hosting complex crater 32 km in diameter centered at 79.3°N, 38.9°E. The black lines outline the north-south band selected for determination of wall slopes. (b) Interpolated MLA coverage color-coded for elevation. Distances are with respect to the crater center. (c) Downslope portions of the northern and southern crater walls for which the slope $\alpha$ is determined.

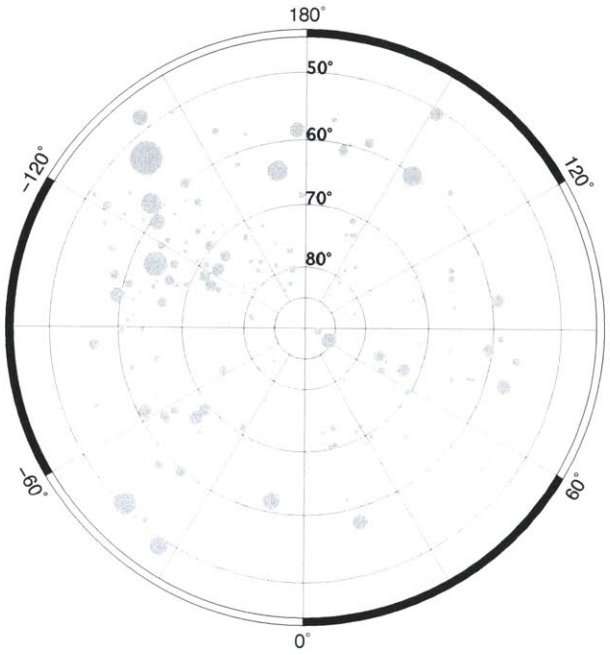


Figure 2-6: North-polar stereographic projection of the location of the craters measured.

## 2.3 Results

### 2.3.1 Survey

The depths and diameters were measured for 537 craters that are morphologically fresh and sufficiently sampled by MLA by mid-February 2012. The latitudinal coverage for these craters extends from 48.7° to 87.8°N (Figure 6), the diameter range spans 1.74 to 207 km, and the depth range spans 0.15 to 4.44 km (Figure 7). Additionally, the floor roughness was measured for 94 of those 537 craters.

The continued activity of the MLA will augment altimetry density and enable the morphometric study of a larger number of craters.

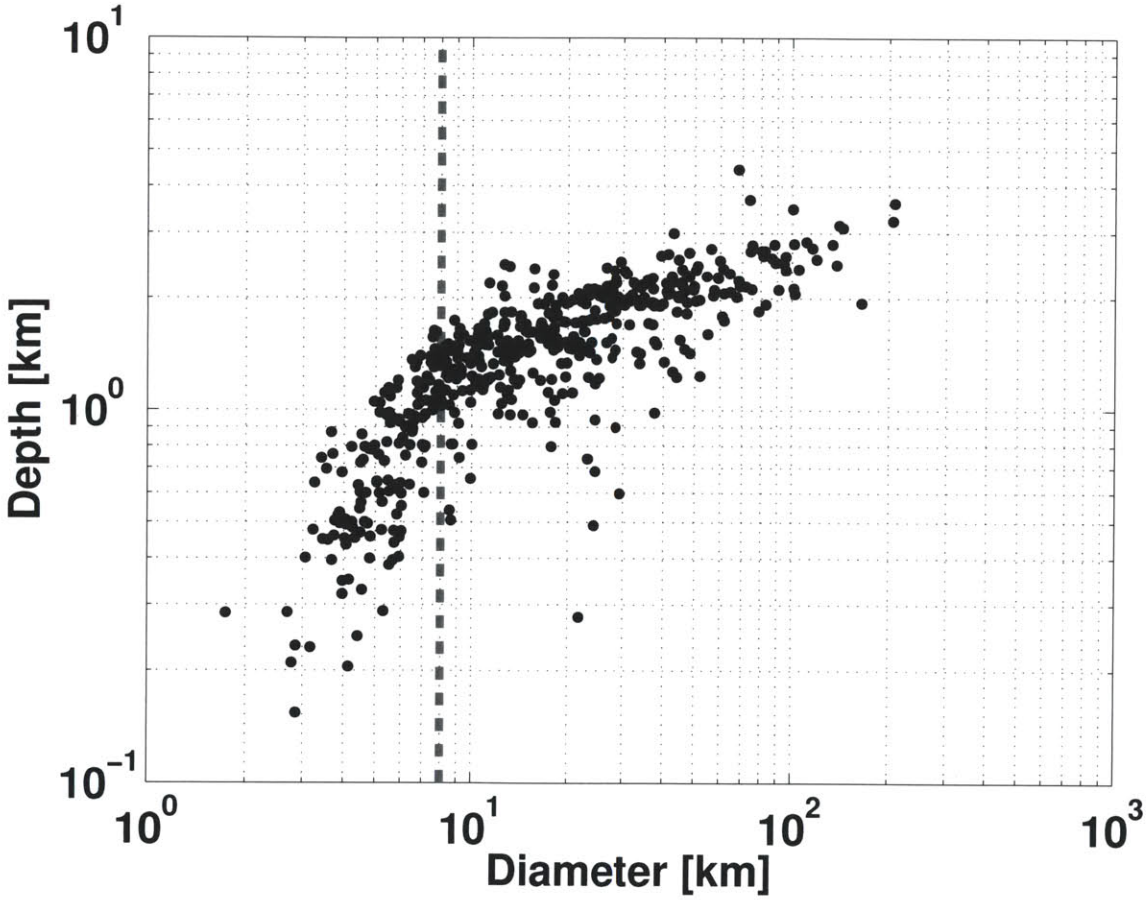


Figure 2-7: Depth versus diameter for the 537 craters characterized in this study. The crater diameter at which craters tend to transition in morphological form between simple and complex craters with increasing diameter is indicated by the dashed line.

### 2.3.2 Crater population classification

#### Radar-bright deposit

The first category for classification is based on radar brightness. A crater is registered as a PDC if it collocates with a radar-bright feature from the most recently acquired radar image of Mercury's north polar region obtained at the Arecibo Observatory [7]. A total of 42 of the 537 craters are so registered as PDCs (Figure 8a). Most craters poleward of 82°N are PDCs [19]. Some large radar-bright features within 4° of the north pole were not included in this population because only a few MLA observations collected from off-nadir operation have been obtained of the area northward of 85°N.

### 2.3.3 Geologic terrain

The second classification category is geological terrain type. The northern volcanic plains (NVP) are a large expanse of smooth plains that occupy the northern lowlands of Mercury, were emplaced shortly after the end of the late heavy bombardment of the inner solar system ~3.8 billion years ago, and cover more than 6% of Mercury's surface [34, 27, 32]. Surrounding the NVP are the generally older and more elevated heavily cratered terrain (HCT), a terrain type usually found in close association with intercrater plains [35].

Of the craters characterized in this study, a total of 327 fall within the boundaries of the NVP as defined by *Head et al.* [34], and 210 are part of the HCT (Figure 8b). The largest craters examined in this study are part of the HCT. In contrast, many of the smaller craters examined are located on the NVP.

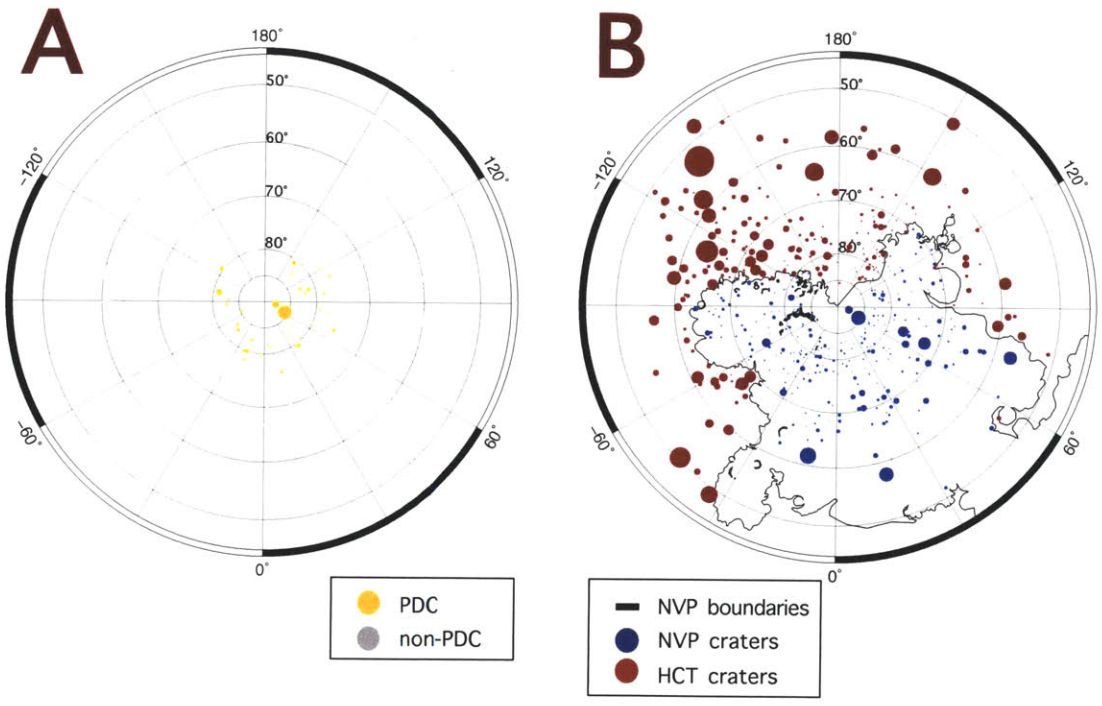


Figure 2-8: The craters of this study divided by two classification schemes; polar stereographic projection. (a) The first classification criterion is whether a crater hosts a radar-bright polar deposit as resolved in the most recent Earth-based radar images of the region [7]. (b) The second classification criterion is whether a crater lies within Mercurys northern volcanic plains (NVP) or in older heavily cratered terrain (HCT).

## 2.4 Interpretation

### 2.4.1 Depth versus diameter

We first examined the relationship between crater depth and diameter for the different crater populations. The relationship between depth and diameter is a first-order measure of crater morphometry and is commonly used in investigating the processes that affect planetary surfaces [36, 37, 38].

To quantify the differences between crater populations, we applied a power law fit to plots of depth as a function of diameter to subsets of craters from each population. The subsets were chosen on the basis of a diameter range common to all populations as well as morphologic homogeneity.

Crater morphology is influenced by the impactor kinetic energy (in addition to the gravitational acceleration and strength of the target body surface, characteristics expected to be common for the craters in our study) and varies in well-documented ways with crater diameter. The craters in this study range from simple bowl-shaped craters to complex craters with a flat floor, a central peak, and slumped wall terraces [39]. Simple craters tend to have larger ratios of depth to diameter than complex craters and the change in crater morphology with diameter is manifested as a change in the slope on a log-log plot of depth versus diameter. *Pike* [36] demonstrated that the morphologic transition between simple and complex craters on Mercury occurs near a diameter of 10 km. For the data set in this study, the transition diameter is about 8 km (Figure 7).

The four populations of craters in this study all included complex craters, but the HCT lacks PDCs in the simple-crater regime. The non-uniform distribution may be explained by the tendency for radar-bright material to be located near one of Mercury's "cold poles" at 90E [18, 21]. To avoid uneven contributions from simple craters in the different crater populations, the power law fit to plots of depth versus

Table 2.1: Depth versus diameter linear fits for the four crater populations. The number of craters used for the linear fit $n$ corresponding to a diameter range between 11 and 50 km, the crater depth $d_f$, the rim-crest diameter $D$, the standard deviation of the difference between the depths and the linear fit $\sigma$ are shown. Figure 2-9 provides an illustration.

| | | non-PDC | PDC | |
|---|---|---|---|---|
| **HCT** | $n$ | 121 | 4 | 125 |
| | $d_f$ | $0.84\ D^{0.21}$ | $1.24D^{0.16}$ | $0.85\ D^{0.21}$ |
| | $\sigma$ | 0.340 | 0.026 | 0.339 |
| | $\sigma_{d/D}$ | 0.035 | 0.026 | 0.035 |
| **NVP** | $n$ | 103 | 31 | 134 |
| | $d_f$ | $0.66\ D^{0.29}$ | $0.53\ D^{0.39}$ | $0.64\ D^{0.31}$ |
| | $\sigma$ | 0.145 | 0.171 | 0.140 |
| | $\sigma_{d/D}$ | 0.029 | 0.025 | 0.028 |
| | $n$ | 224 | 35 | |
| | $d_f$ | $0.77\ D^{0.24}$ | $0.54\ D^{0.39}$ | |
| | $\sigma$ | 0.288 | 0.175 | |
| | $\sigma_{d/D}$ | 0.033 | 0.025 | |

diameter was applied only to the complex craters in each population that have a diameter between 11 and 50 km (Figure 8 and Table 1).

### HCT craters versus NVP craters

At a given diameter $D$, the full population of craters in the HCT has a wider range in depth $d$ than does the comparable population of craters in the NPV (Figure 8). This generalization is also indicated by the larger standard deviation $\sigma$ of the observed depth d minus the depth $d_f$ predicted by the power law fits (Table 1).

This dispersion in $d$ can be explained by considering the difference in age of the terrains and the evolution of the cratering flux [35]. The emplacement of the northern smooth plains over an older cratered surface is thought to have occurred at $\sim$ 3.8 G.y. [34], similar to the time of emplacement of smooth plains within and exterior to the Caloris basin [40]. Such a time postdated the pre-Tolstojan [35], the epoch during which the impact flux was the highest [41]. In particular, most of the craters on the NVP formed after the end of the late heavy bombardment of the inner solar system

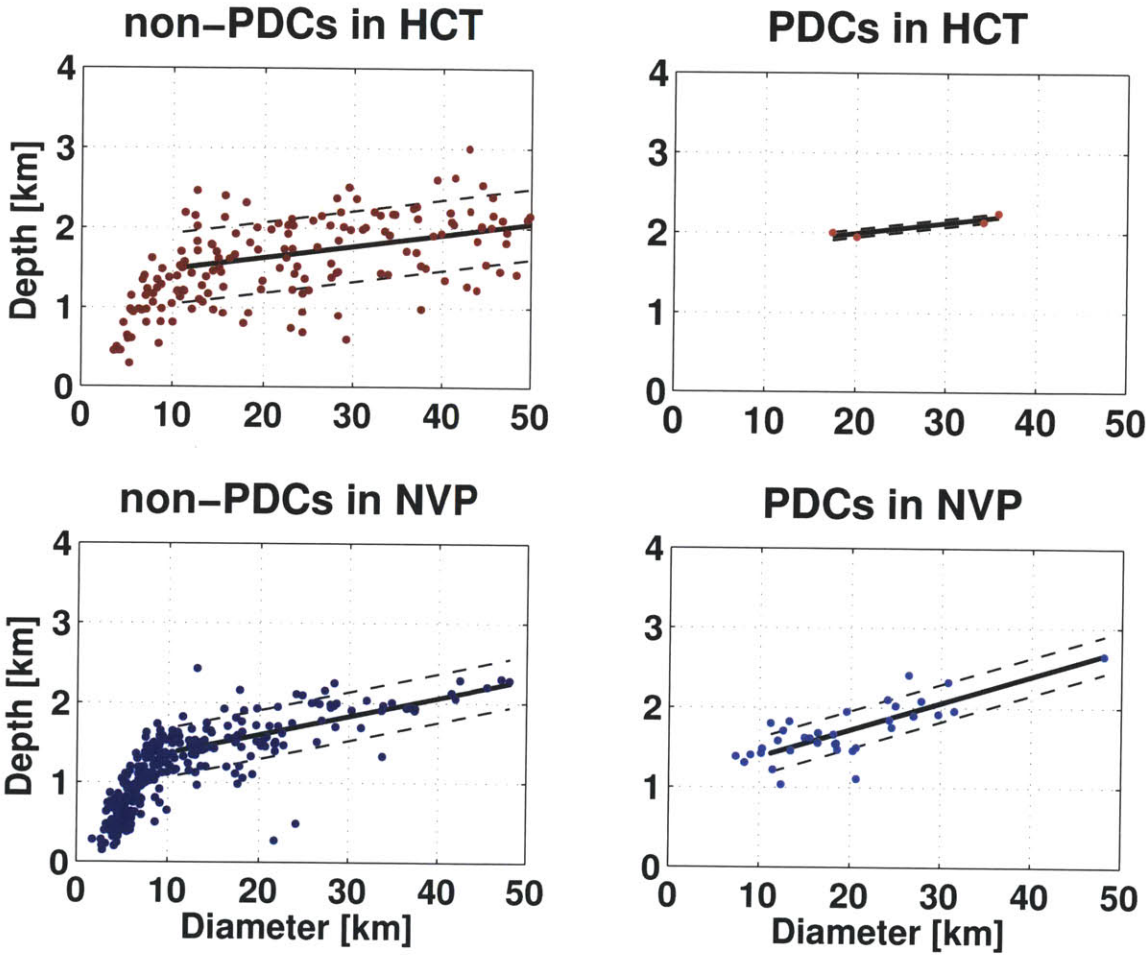


Figure 2-9: Depth versus diameter for the four different crater populations in this study. The thick lines denote power law fits to the data points for complex craters between 11 and 50 km in diameter; one standard deviations are denoted by the dashed lines.

[40], whereas the surface of the HCT includes the effects of numerous impacts that occurred during the late heavy bombardment.

Processes that acted to modify $d$ included subsequent impacts on or near crater rims, deposition of impact ejecta onto crater floors, and downslope motion of craters walls and central peaks driven by micrometeoroid bombardment, seismic shaking, and other effects [42]. The same processes also contributed to enlarging the diameter $D$, but their effect on $D$ is small compared with that on $d$.

Because the cumulative effect of modification processes on crater shape increases with the time exposed to impact bombardment, the population of craters in the HCT includes more degraded examples than the population of craters on the NVP. This difference accounts for the greater dispersion in $d$ at a given $D$ for the HCT than for the NVP.

### PDC versus non-PDC

We used a statistical tool to test the differences in $d/D$ for samples of PDCs and non-PDCs. The statistical test performed is the Wilcoxon rank-sum test (also known as the Mann-Whitney test), a variant of the Students-t test applied in comparisons of crater populations by Barlow et al. [23] and Vilas et al. [26]. We selected samples of craters on the basis of a diameter range for which the crater density was similar for the PDC and non-PDC populations. The diameter range spanned 10 to 35 km and includes 33 PDCs and 200 non-PDCs. The Wilcoxon rank-sum test compares whether two samples of unequal sizes come from identical populations without making specific assumptions about the form of the underlying population distribution [43]. This test was chosen because the Students-t test requires that the samples be normally distributed, which is an invalid assumption for this comparison because the samples fail the $\chi^2$ test at the 95% significance level. The resulting calculated p-value of 0.38 is outside the rejection region. The rejection region spans from 0 to 0.05 for the 95%

significance level. The Wilcoxon rank-sum test therefore indicates that the $d/D$ ratios of PDC and non-PDC samples are not statistically different at the 95% significance level.

Moreover, the smaller standard deviation $\sigma_{d/D}$ of $d/D$ ratios for PDCs implies that the $d/D$ ratio is more constrained, indicating a less variable morphology. In particular, crater rims for the PDCs are more consistent in their elevation and more nearly circular and concentric to the crater centers (Table 1). Denser MLA coverage at high latitudes could also lead to smaller values of $\sigma_{d/D}$, because for a given range of values used to assess a measurement (e.g., the range of depth values is 0.03 km in Figure 3b), a large number of points reduces the associated standard variation. However, non-PDCs at similar latitudes have higher ?d/D values than PDCs. By arguments similar to those applied above, the lower $\sigma_{d/D}$ for PDCs suggests that crater modification processes operated over less accumulated time than for the population of non-PDCs sampled here. In other words, the PDCs may on average be younger than the non-PDCs at comparable high northern latitudes.

### Comparison with past morphometric study

We compared the morphometry of nine of the 12 PDCs assessed in [26] with the morphometry estimated in this study (Figure 10). The three remaining PDCs are the northernmost (above MESSENGER's orbit inclination) craters and are not compared because of insufficient MLA coverage.

The diameter values are similar except for craters M2 and L2 which have photoclinometric-derived diameters substantially larger than the MLA-derived diameters. Large portions of both rims are overlaid with other craters, which may have resulted in a discrepancy in defining the crater rim position and therefore in estimating the diameter. The depths of four PDCs from Vilas [26] are smaller than 75% of the equivalent altimetry-derived values, but no systematic error appears to exist and the inconsis-

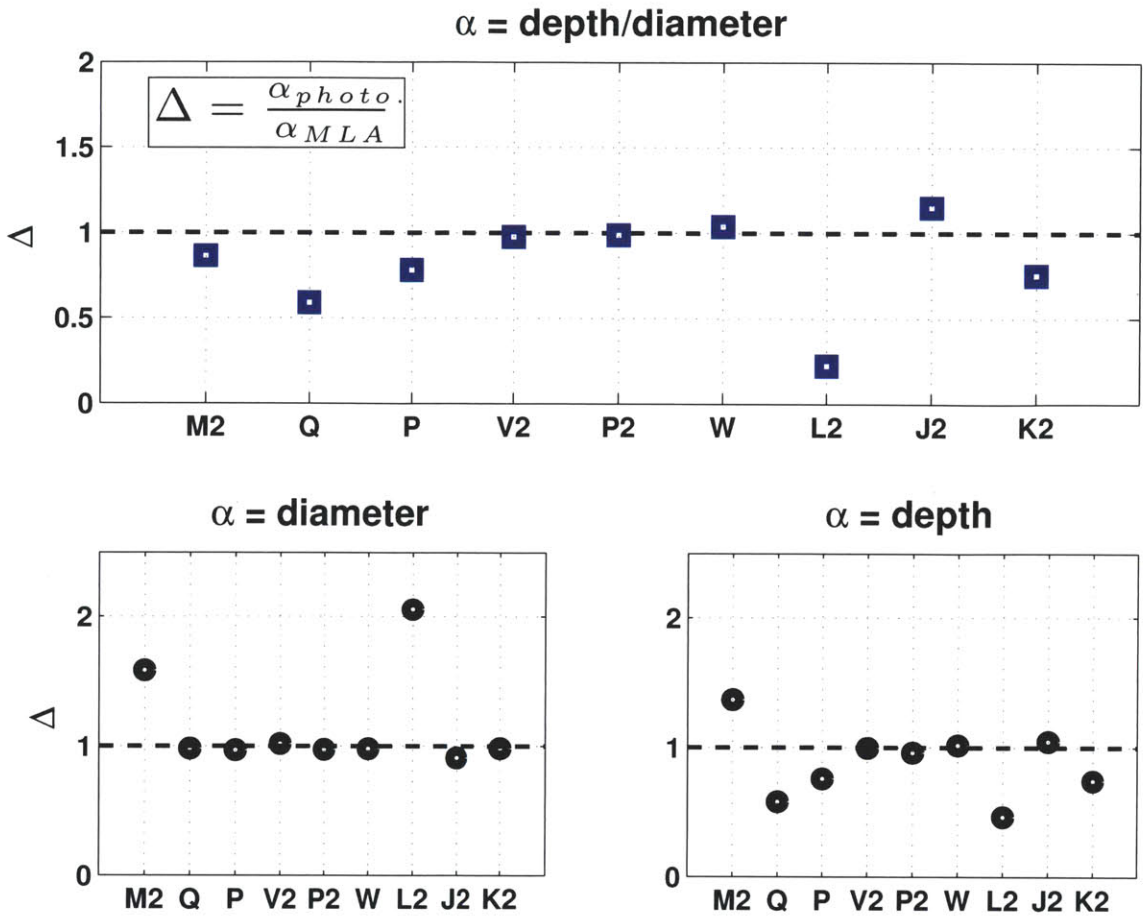


Figure 2-10: Comparison of crater morphometry for the nine PDCs assessed via photoclinometry in Vilas [26] and MLA-derived topography in this study.

tency may be due to the better accuracy and precision of the altimetry-based method. As a result, the depth-to-diameter ratios for seven of the nine PDCs are smaller for craters measured by Vilas [26].

### 2.4.2 Other morphometric measurements

We examined the ratios of the slopes of the southward-facing (northern) and northward-facing (southern) walls for 30 PDCs sufficiently well sampled by altimetry. No systematic difference in wall slope was found, as indicated by a mean slope ratio of ~1 (Figure 11a). Because radar-bright material tends to be concentrated on northward-facing slopes for craters at high northern latitudes, such material has no detectable

effect on wall slope.

Walls are steepest for smaller (< 20 km diameter) complex craters (Figure 11b), which is as expected considering that such craters are closer to the transition diameter from simple to complex craters. In general, slopes are far below the angle of repose predicted for regolith material ( 35°) [44].

The Wilcoxon rank-sum test was applied to floor roughness values for complex crater floors over three baselines. The calculated p-values for the comparison between the PDC and non-PDC samples at the 0.8-, 3.2- and 5.6-km baselines are 0.234, 0.112 and 0.640 respectively, all above the comparison value of 0.05 for the 95% significance level (i.e., outside the rejection region spanning 0 to 0.05). The test therefore indicates that there is no resolvable difference in roughness between the floors of PDCs and non-PDCs. The median differential slope values are somewhat higher for small craters at the largest baseline ($L = 5.6$ km) because the slope measurements include points for which the footprints sampled the crater wall, which imparted an elevation bias to the slope measurement (Figure 12).

Furthermore, no discernible difference is detected when comparing floor roughness across all population at the three baselines examined (Figure 2-12).

## 2.5 Conclusion

We refer to the two questions posed in the introduction.

### 2.5.1 What does a systematic survey of crater morphometry indicate about the north polar region of Mercury?

- The NVP craters have been subjected to less extensive crater modification processes, on average, than HCT craters. The NVP crater population displays a smaller dispersion in $d/D$ values and marginally greater values of d at a given

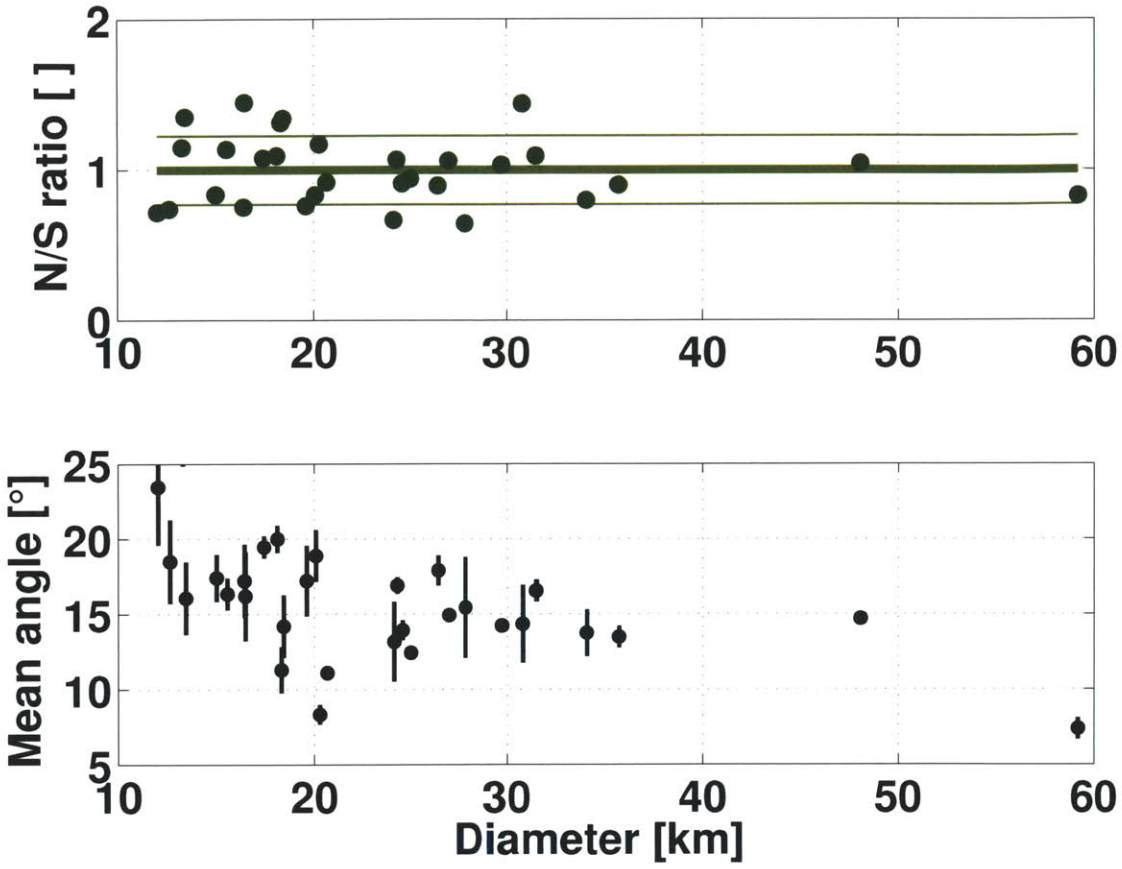


Figure 2-11: Wall slope angles versus crater diameter for the 30 PDCs sufficiently well sampled by altimetry data. (a) The ratio of northern wall slope to southern wall slope. The mean ratio is denoted by the thick horizontal line and one standard deviation is denoted by the thin horizontal lines. (b) Mean wall slope angle versus crater diameter for the same population of PDCs. The mean slope angle is the average of the northern and southern wall slope values; the two slope angles are indicated by the ends of the vertical lines through each mean value.

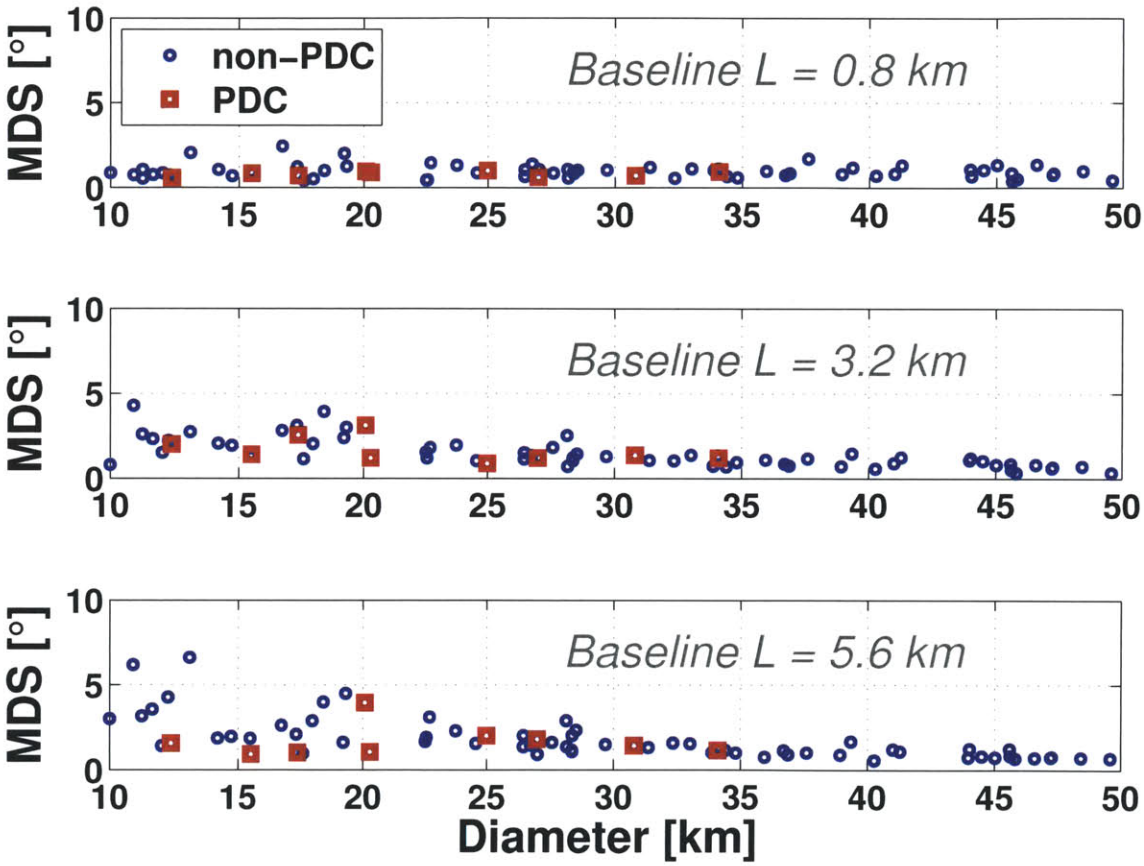


Figure 2-12: Absolute value of median differential slope (MDS) for 94 craters sufficiently large to display a generally flat crater floor.

$D$, and it includes more simple craters sufficiently well preserved to be measured by MLA, than does the HCT crater population.

- PDCs measured in this study appear less degraded, on average, than non-PDCs. The PDCs have a better-preserved morphology (larger $d/D$) regardless of geographic location than non-PDCs. the impacting frequency started to decrease and therefore the PDC experienced less of the impact-driven degradation processes.

- Radar-bright material is located preferentially in younger craters.

### 2.5.2 Does the radar-bright material affect the morphology of the polar-deposit-hosting craters?

- Slopes of crater walls are similar for PDCs in northward-facing and southward-facing directions. Radar-bright material thus has no detectable effect on wall slope.

- Radar-bright material has no detectable influence on the roughness of the floors of complex craters at the baselines studied (0.8 to 5.6 km).

- Radar-bright material has no detectable influence on crater morphometry. There is thus no need to invoke thick layers of water ice admixed with non-volatile material, in contrast with the conclusion of [26]. The inconsistency between the crater morphometry assed by the two methods doesn't appear to be systematic and may be due to the higher accuracy and precision of altimetry-derived measurements compared with the topographic information derived from Mariner 10 imaging data.

- An upper limit on the thickness of radar-bright material on the floors of PDCs is provided by the specifications of the MLA instrument. The MLA measures

elevation with a 1-m precision, but detecting the layer of radar-bright material requires comparing the elevation over a number of consecutive altimetry footprints. MLA's 20-m vertical accuracy with respect to Mercury's center of mass limits the comparison of the elevation of consecutive altimetry footprints and therefore the detectability of a layer of radar-bright material thinner than 20 m.

# Chapter 3

# Simple-to-complex crater regime transition

## 3.1 Background

The shape of impact craters on a body depends on the kinetic energy of the impactors. Impactors with higher kinetic energy form crater shapes of greater morphologic complexity. This morphologic evolution is tracked as a function of crater diameter; specific crater morphologies are binned in crater diameter ranges (Figure 1).

Broadly speaking, morphologic categories progress from the simple regime for the smallest impacts to the complex and ultimately basin regime for the largest impacts [39]. A simple crater is best described by a paraboloid. A complex crater is a deformed simple crater; the walls contain slumped terraces and the floor is flat with a protruding central peak. Basins have less defined crater rims enclosing a number of annulated formations, central peak mounts and expanses of impact-produced melts.

Each morphologic transition is accompanied by a change in the depth-to-diameter relationship. The slope of the depth-to-diameter ratio of a particular morphologic regime decreases with increasing crater diameter. This results in an inflection in

the depth versus diameter plot, from which the value of the transition diameters is inferred (Figure 2).

The rheological mechanisms that shape an impact crater are dependent on the body's gravity and surface yield strength [45]. As such, the set of transition diameters separating crater morphologies are unique to a particularly body, even though the functional form of the depth-to-diameter relationships remains the same.

Past morphometric studies used photoclinometric techniques to assess the diameter and depth of a crater [46]. Relative topographic elevations, such as rim height with respect to its associated crater floor, are calculated from shadow lengths, knowledge of ephemerides, and spacecraft attitude (i.e., viewing angles and range to a reference surface). This technique has served as a basis to characterize the morphometry of impact craters on Mercury [36, 23], the Moon [46], Mars [25, 24], and icy bodies [47, 48]. Morphometric studies have yielded a simple-to-complex transition diameter of 10 kilometer on Mercury [36] and 16 kilometer on the Moon [46].

Altimeters have recently been onboard missions to the Moon [49], Mars smith2001, 433 Eros [50], and Mercury [27]. Altimetry-derived measurements of a surface provide geodetically-controlled topography that have small margin of errors and avoid the bias of shadow length measurement. These high-resolution topographic datasets have been used to revisit studies of crater morphometry at the simple-to-complex [51] and complex-to-basin [52] transitions on the Moon, examine the influence of subsurface ice on crater relaxation on Mars [37] and radar-bright deposits on craters at Mercurys north polar region (see Chapter 1), etc.

In this study, we are interested in reconstructing the depth versus diameter plots of simple and complex craters and consequently in determining the value of the simple-to-complex transition diameter from altimetry-derived datasets of the Moon and Mercury.

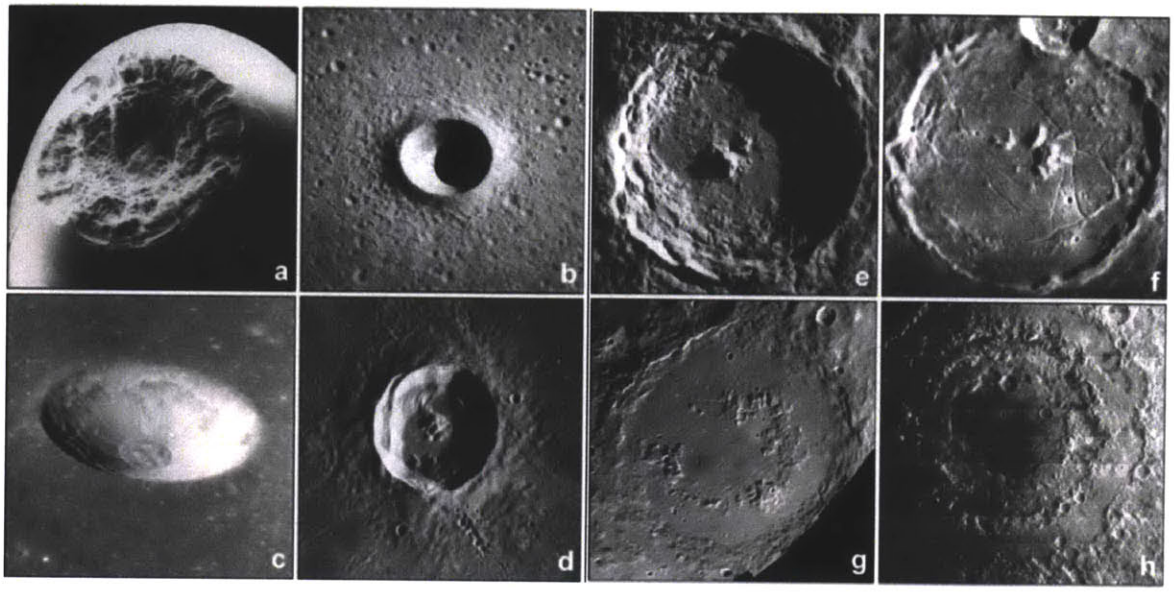


Figure 3-1: The different crater morphologies as a function of diameter. Figure reproduced from [53].

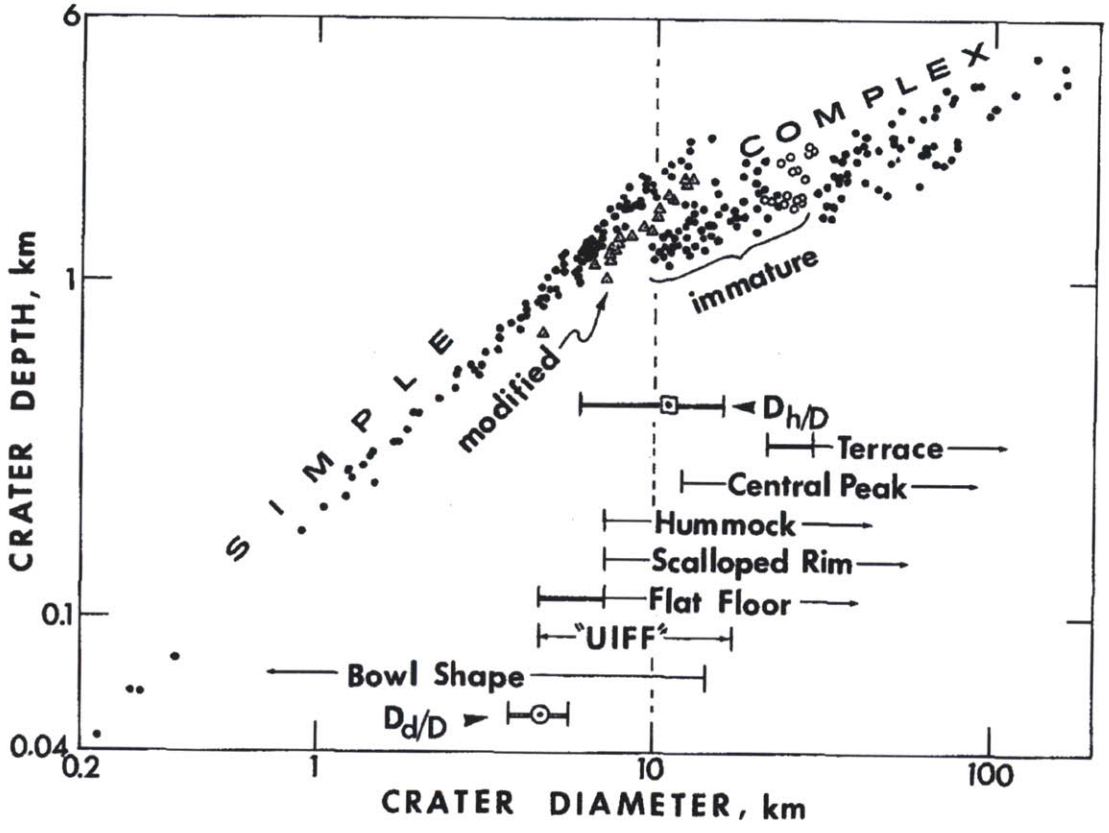


Figure 3-2: Log-log of depth versus diameter of craters from photoclinometric studies compiled by Pike from Mariner 10 images [36]. Figure reproduced from Pike [36].

## 3.2 Morphometric measurements

We measure the two fundamental geometric properties of craters: depth and diameter. Crater depth is found from the elevation difference between the crater floor and the rims. The crater rims are defined as the transition between the ejecta blanket and the crater interior; the rims are the highest topographic points of a crater. Crater diameter is the diameter of a least squares best fit circle applied to the half of rim locations with the highest elevation because topography-reducing processes (meteoritic gardening and solar wind driving landscape diffusion, subsequent impacts obliterating rims, etc.) are more effective than topography-adding processes (ejecta blanketing operating preferentially on the walls, which is unlikely). These definitions apply to craters on the Moon and Mercury, but the two differing altimetry datasets result in functionally different methods.

The lunar crater measurements are computed from the high-resolution surface grids interpolated from LOLA tracks (1024 pixel-per-degree Lunar Digital Elevation Models). Crater locations are selected from an existing dataset of locations and approximate crater diameter compiled from Crater Detection Algorithms [54]. We recalculate the crater diameter so that each diameter value comes from a computation similar in nature to that applied to craters on Mercury. To define rim locations, we first extend fifty radial profiles from the datasets crater center to twice the datasets crater radius. The radial profiles are spaced angularly by a constant azimuthal angle ($360/50 = 7.2°$) to complete a full disk of coverage and each radial profile has an associated rim location. The rim elevations are subtracted from the average of the lowest half of the floor points. Qualitative inspection of crater morphometry removes craters with mismatching morphometric measurements. Such mismatches include the use of neighboring topographic highs not associated with the crater rims, which introduces a bias in calculating the rim height and hence the crater depth.

Assessing the morphometry of craters on Mercury relies directly on the altimetry

tracks of the MLA. Indeed, the coverage is insufficient to produce interpolated grids for craters at lower latitudes where the spacing between ground tracks is significantly larger than near the north pole. The rim locations are therefore selected from the most crater-centric altimetry tracks, i.e., the tracks that include a significant portion of the crater floor and hence two portions of the walls that are separated by a distance close to the true value of the crater diameter. Furthermore, the altimetry points used in assigning the depth of a floor are manually selected to avoid the bias of superposed craters. Crater images extracted from a global mosaic compiled by MESSENGER Dual Imaging System images [30] are used to corroborate the MLA-derived measurements or discard craters with mismatching morphometric properties. Common mismatches are the least squares best fit circle yielding a crater diameter that doesnt follow the physical crater diameter and floor depths that are selected from altimetry shots of the crater walls instead of the floor due to insufficient coverage.

## 3.3 Planetary comparison

The depth versus diameter graphs show the inflection in depth-to-diameter slope (Figure 3). We selected a subset of the freshest craters to examine the upper envelope by discarding shallower craters, which have been affected by degradation mechanisms that reduce the depth of a crater of a given diameter and/or increase its diameter, resulting in smaller depth-to-diameter ratios [42]. Indeed, in a surface-wide survey of crater morphometry, the range of crater depth for a given crater diameter would span from just above 0 km (for the shallowest, most degraded craters) to the depth of the freshest, least modified craters. We are interested in the functional form of the depth to diameter for the freshest craters and therefore only select the subset of craters with greatest depth for a given diameter. As such only the top envelope of crater points is selected.

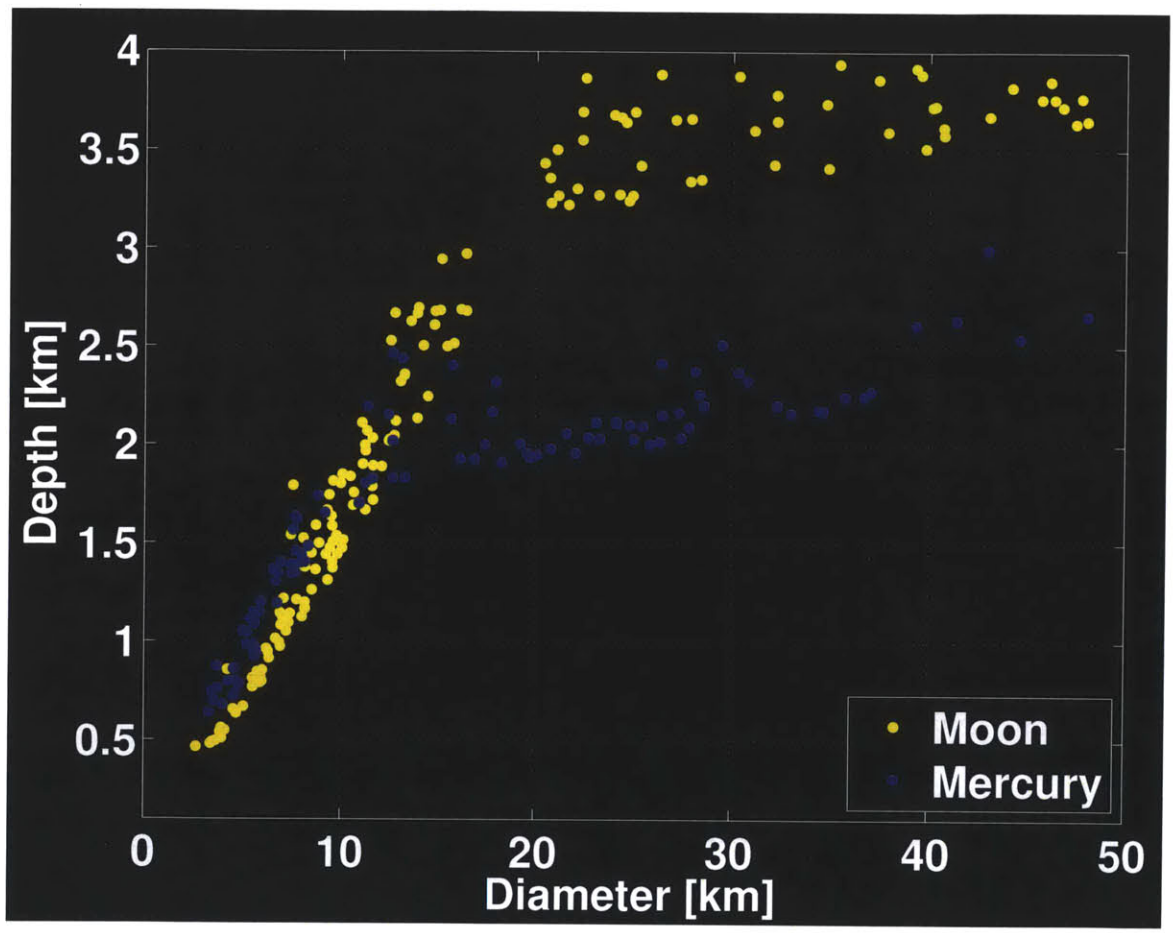


Figure 3-3: Depth versus diameter plot for fresh craters on Mercury and the Moon based on altimetry-derived measurements.

The transition diameter for lunar craters is 16 km, in line with previous studies. The transition diameter for craters on Mercury is near 8 km, 2 km lower than established by [36]. The difference may be due to the higher accuracy of measurements achieved with altimetry-derived methods versus photoclinometric techniques.

The behavior of simple craters is similar for both bodies and corresponds with the d/D $\sim$ 0.2 linear approximation for simple craters [36]. This approximation is also a representation of the fact that strength-dominated mechanisms operate at the simple regime. The silicate crust is strong enough to support the transient cavity that is formed from the hemispherical excavation of material that occurs during the unloading of the pressure waves [39].

The transition to complex morphology is initiated when the transient cavity cant be fully supported; the mass needs to be redistributed in a more energetically stable shape. The strength-dominated regime is overtaken by gravity-dominated regime, in which the surface gravity attenuates the processes that influence the final crater shape. The transition diameter $D_t$ is formulated in [45],

$$D_t = 9.0\frac{Y}{\rho g} \tag{3.1}$$

where $Y$ is surface yield strength, $\rho$ the surface density and $g$ the surface gravity. To first order, both the surface density $\rho$ and yield strength Y can be assumed constant because bodies have a silicate crust. The surface gravity term varies the most. Mercurys surface gravity ($3.7\frac{m}{s^2}$) is 2.3 times greater than the Moons ($1.6\frac{m}{s^2}$) and means that gravity-dominated mechanisms overtake strength-dominated mechanisms at smaller impactor kinetic energies (i.e., at smaller crater diameters). This explains why the transition diameter and the depth of the complex craters are both smaller for Mercury than on the Moon because Mercurys surface gravity is 2.3 times higher than the Moons (Figure 4).

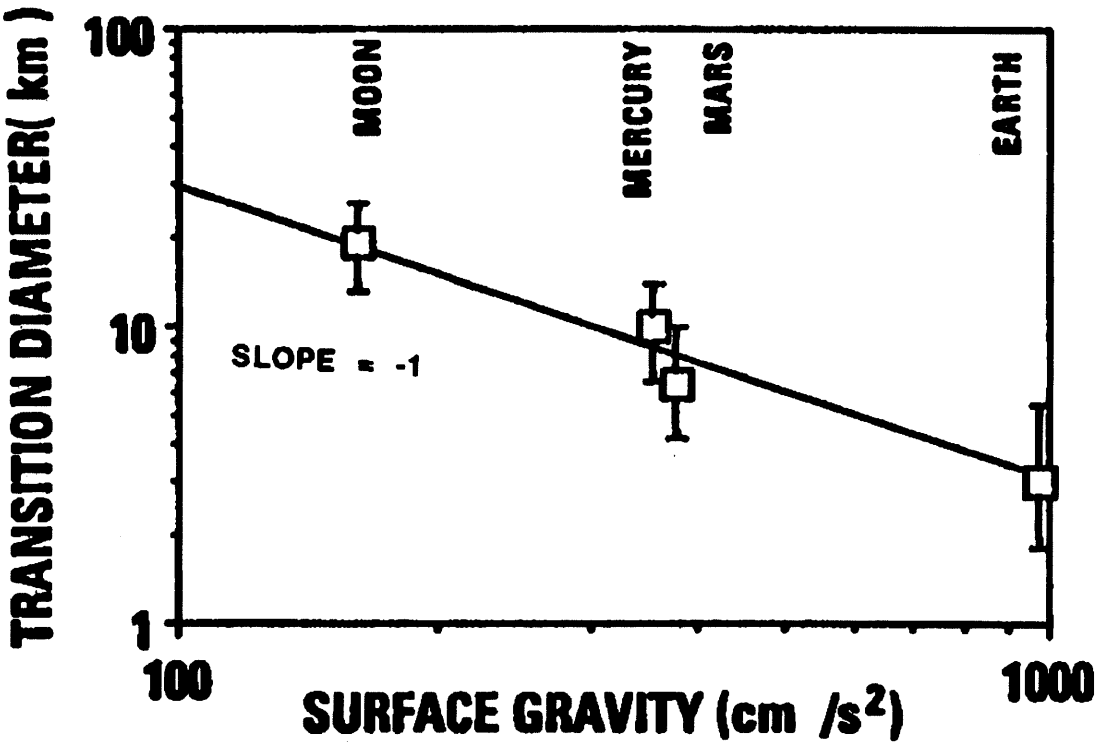


Figure 3-4: Transition diameter as a function of surface gravity determined from photoclinometric studies [45]. Figure reproduced from *O'Keefe and Ahrens* [45] with data from *Schenk* [47].

# Bibliography


[1] B. J. Butler, D. O. Muhleman, and M. A. Slade. Mercury: Full-disk radar images and the detection and stability of ice at the north pole. *J. Geophys. Res.*, 98:15,003–15,023, 1993.

[2] B. J. Butler, D. O. Muhleman, and M. A. Slade. VLA/Goldstone 3.5-cm radar observations of Mercury in 1994: South polar and other results. *Bull. Am. Astron. Soc.*, 26:1,106, 1994.

[3] J. K. Harmon and M. A. Slade. Radar mapping of Mercury: Full-disk delay-Doppler images. *Science*, 258:640–643, 1992.

[4] M. A. Slade, B. J. Butler, and D. O. Muhleman. Mercury radar imaging: Evidence for polar ice. *Science*, 258, 1992.

[5] J. K. Harmon, P. J. Perillat, and M. A. Slade. High-resolution radar imaging of Mercury's north pole. *Icarus*, 149:1–15, 2001.

[6] J. K Harmon, M. A. Slade, R. A. Vlez, A. Crespo, M. J. Dryer, and J. M. Johnson. Radar mapping of Mercury's polar anomalies. *Nature*, 369:213–215, 1994.

[7] J. K. Harmon, M. A. Slade, and M. S. Rice. Radar imagery of Mercury's putative polar ice: 1999-2005 Arecibo results. *Icarus*, 211:37–50, 2011.

[8] A. E. Potter. Chemical sputtering could produce sodium vapor and ice on Mercury. *Geophys. Res. Lett.*, 22:3,289–3,292, 1995.

[9] R. M. Killen, J. Benkhoff, and T. H. Morgan. Mercury's polar caps and the generation of an HO exosphere. *Icarus*, 125:195–211, 1997.

[10] J. I. Moses, K. Rawlins, K. Zahnle, and L. Dones. External sources of water for Mercury's putative ice deposits. *Icarus*, 137:197–221, 1998.

[11] A. L. Sprague, D. M. Hunten, and K. Lodders. Sulfur at Mercury, elemental at the poles and sulfides in the regolith. *Icarus*, 118:211–215, 1995.

[12] L. Starukhina. Water detections on atmosphereless celestial bodies: Alternative explanations of the observations. *J. Geophys. Res.*, 106:14,70114,710, 2001.

[13] D. A. Paige, S. E. Wood, and A. R. Vasavada. The thermal stability of water ice at the poles of Mercury. *Science*, 258:643–646, doi:10.1126/science.258.5082.643, 1992.

[14] A. P. Ingerstoll, T. Svitek, and B. C. Murray. Stability of polar frosts in spherical bowl-shaped craters on the Moon, Mercury, and Mars. *Icarus*, 100:40–47, 1992.

[15] A. R. Vasavada, D. A. Paige, and S. E. Wood. Near-surface temperature on Mercury and the Moon and the stability of polar ice deposits. *Icarus*, 141:179–193, 1999.

[16] L. R. Nittler, R. D. Starr, S. Z. Weider, T. J. McCoy, W. V. Boynton, D. S. Ebel, C. M. Ernst, L. G. Evans, J. O. Goldsten, D. K. Hamara, D. J. Lawrence, R. L. McNutt Jr., C. E. Schlemm II, S. C. Solomon, and A. L. Sprague. The major-element composition of Mercury's surface from MESSENGER X-ray spectrometry. *Science*, 333:1,847–1,849, 2011.

[17] G. A. Neumann, J. F. Cavanaugh, X. Sun, E. Mazarico, D. E. Smith, M. T. Zuber, S. C. Solomon, and D. A. Paige. Dark material at the surface of polar crater deposits on Mercury. In *LPSC XXXIII*, Abstract 2651, 2012.

[18] N. L. Chabot, C. M. Ernst, B. W. Denevi, J. K. Harmon, S. L. Murchie, D. T. Blewet, S. C. Solomon, , and E. Zhong. Areas of permanent shadow in Mercurys south polar region ascertained by MESSENGER orbital imaging. *Geophys. Res. Lett.*, 39, 2012.

[19] M. J. Chabot, C. M. Ernst ad J. K. Harmon, S. L. Murchie, S. C. Solomon, D. T. Blewett, and B. W. Denevi. Craters hosting radar-bright deposits in Mercury's north polar region. In *LPSC XXXXIII*, Abstract 1476, 2012.

[20] J. A. Zhang and D. A Paige. Cold-trapped organic compounds at the poles of the Moon and Mercury: Implications for origins. *Geophys. Res. Lett.*, 36, 2009.

[21] D. A. Paige, M. A. Siegler, J. K. Harmon, D. E. Smith, M. T. Zuber, G. A. Neumann, and S. C. Solomon. Thermal stability of frozen volatiles in the north polar region of Mercury. In *LPSC XXXXIII*, Abstract 2875, 2012.

[22] J. F. Cavanaugh, J. C. Smith, X. Sun, A. E. Bartels, L. Ramos-Izquierdo, D. J. Krebs, J. F. McGarry, R. Trunzo, A. M. Novo-Gradac, J. L. Britt, J. Karsh, R. B. Katz, A. T. Lukemire, R. Szymkiewicz, D. L. Berry, J. P. Swinski, G. A. Neumann, M. T. Zuber, and D. E. Smith. The Mercury Laser Altimeter instrument for the MESSENGER Mission. *Space Sci. Rev.*, 131:451–479, 2007.

[23] N. G. Barlow, R. A. Allen, and F. Vilas. Mercurian impact craters: Implications for polar ground ice. *Icarus*, 141:194–204, 1999.

[24] S. W. Squyres and M. H. Carr. Geomorphic evidence for the distribution of ground ice on Mars. *Science*, 231, 1986.

[25] M. J. Cintala and P. J. Mouginis-Mark. Martian fresh crater depths: More evidence for subsurface volatiles? *Geophys. Res. Lett.*, 7:329–332, 1980.

[26] F. Vilas, P. S. Cobian, N. G. Barlow, and S. M. Lederer. How much material do the radar-bright craters at the Mercurian poles contain? *Planet. and Space Sci.*, 53, 2005.

[27] M. T. Zuber, D. E. Smith, R. J. Phillips, S. C. Solomon, G. A. Neumann, S. A. Hauck II, S. J. Peale, O. S. Barnouin, J. W. Head, C. L. Johnson, F. G. Lemoine, E. Mazarico, X. Sun, M. H. Torrence, A. M. Freed, C. Klimczak, J.-L. Margot, J. Oberst, M. E. Perry, R. L. McNutt Jr., J. A. Balcerski, N. Michel, M. J. Talpe, and D. Yang. Topography of the northern hemisphere of Mercury from MESSENGER Laser Altimetry. *Science Report*, 2012.

[28] D. E. Smith, M. T. Zuber, G. B. Jackson, J. F. Cavanaugh, G. A. Neumann, H. Riris, X. Sun, R. S. Zellar, C. Coltharp, J. Connelly, R. B. Katz, I. Kleyner, P. Liiva, A. Matuszeski, E. M. Mazarico, J. F. McGarry, A.-M. Novo-Gradac, M. N. Ott, C. Peters, L. A. Ramos-Izquierdo, L. Ramsey, D. D. Rowlands, S. Schmidt, V. S. Scott III, G. B. Shaw, J. C. Smith, J.-P. Swinski, M. H. Torrence, G. Unger, A. W. Yu, and A. W. Zagwodzki. The Lunar Orbiter Laser Altimeter investigation on the Lunar Reconnaissance Orbiter mission. *Space Sci. Rev.*, 150:209–241, 2010.

[29] S. E. III Hawkins, J. D. Boldt, E. H. Darlington, R. Espiritu, R. E. Gold, B. Gotwols, M. P. Grey, C. D. Hash, J. R. Hayes, S. E. Jaskulek, C. J. Kardian, M. R. Keller, E. R. Malaret, S. L. Murchie, P. K. Murphy, K. Peacock, L. M. Prockter, R. A. Reiter, M. S. Robinson, E. D. Schaefer, R. G. Shelton, R. E. Sterner, H. W. Taylor, T. R. Watters, and B. D. Williams. The Mercury Dual Imaging System on the MESSENGER spacecraft. *Space Sci. Rev.*, 131:247–338, 2007.

[30] K. J. Becker, M. S. Robinson, T. L. Becker, L. A. Weller, S. Turner, L. Nguyen, C. Selby, B. W. Denevi, S. L. Murchie, R. L. McNutt, and S. C. Solomon. Near global mosaic of Mercury. In *Eos Trans. AGU, 90 (52), Fall Meet. Suppl.*, Abstract P21A-1189, 2009.

[31] M. A. Kreslavsky and J. W. Head III. Kilometer-scale roughness of Mars: Results from MOLA data analysis. *J. Geophys. Res.*, 105:26,695–26,711, 2000.

[32] D. Yang, G. A. Neumann, M. T. Zuber, and S. C. Solomon. Distribution of surface slopes and roughness in Mercury's northern hemisphere. In *Eos Trans. AGU, 90 (52), Fall Meet. Suppl.*, Abstract P41A-1577, 2011.

[33] M. A. Rosenburg, O. Aharonson, J. W. Head, M. A. Kreslavsky, E. Mazarico, G. A. Neumann, D. E. Smith, M. H. Torrence, and M. T. Zuber. Global surface slopes and roughness of the Moon from the Lunar Orbiter Laser Altimeter. *J. Geophys. Res.*, 116, 2011.

[34] J. W. Head, C. R. Chapman, R. G. Strom, C. I. Fassett, B. W. Denevi, D. T. Blewett, C. M. Ernst, T. R. Watters, S. C. Solomon, S. L. Murchie, L. M. Prockter, N. L. Chabot, J. J. Gillis-Davis, J. L. Whitten, T. A. Goudge, D. M. H. Baker, D. M. Hurwitz, L. R. Ostrach, Z. Xiao, W. J. Merline, L. Kerber, J. L. Dickson, J. Oberst, P. K. Byrne, C. Klimczak, and L. R. Nittler. Flood volcanism in the northern high latitudes of Mercury revealed by MESSENGER. *Science*, 333:1,853–1,856, 2011.

[35] P. D. Spudis and J. E. Guest. Stratigraphy and geologic history of Mercury. In F. Vilas, C. R. Chapman, and M.S. M. S. Matthews, editors, *Mercury*. The University of Arizona Press, Tucson, AZ, 1988.

[36] R. J. Pike. Geomorphology of impact craters on Mercury. In F. Vilas, C. R. Chapman, and M. S. Matthews, editors, *Mercury*, pages 165–273. The University of Arizona Press, Tucson, 1988.

[37] J. B. Garvin, S. E. H. Sakimoto, J. J. Frawley, and C. Schnetzler. North polar region craterforms on Mars: Geometric characteristics from the Mars Orbiter Laser Altimeter. *Icarus*, 144:329–352, 2000.

[38] P. M. Schenk and E. P. Turtle. Europas impact craters: Probes of the icy shell. In R. T. Pappalardo, W. B. McKinnon, and K. Khurana, editors, *Europa*. The University of Arizona Press, Tucson, 2009.

[39] H. J. Melosh. *Impact Cratering: A Geologic Process*. Oxford University Press, New York, 1989.

[40] R. G. Strom, M. E. Banks, C. R. Chapman, C. I. Fassett, J. A. Forde, J. W. Head III, W. J. Merline, L. M. Prockter, , and S. C. Solomon. Mercury crater statistics from MESSENGER flybys: Implications for stratigraphy and resurfacing history. *Planet. Space Sci.*, 59:1,9601,967, 2011.

[41] G. Neukum, J. Oberst, H. Hoffman, R. Wagner, and B. A. Ivanov. Geologic evolution and cratering history of Mercury. *Planet. Space Sci.*, 49:1,507–1,521, 2001.

[42] J. W. Head III. Processes of lunar crater degradation: Changes in style with geologic time. *The Moon*, 12:299–329, 1975.

[43] Devore J. L. *Probability and Statistics for Engineering and the Sciences*. Brooks/Cole, 2007. Monterey, CA.

[44] A. Van Burkalow. Angle of repose and angle of sliding friction: An experimental study. *Geol. Soc. Am. Bull.*, 56:669–707, 1945.

[45] J. D O'Keefe and T. J. Ahrens. Planetary cratering mechanisms. *J. Geophys. Res.*, 98:17,001–17,028, 1993.

[46] R. J. Pike. Formation of complex impact craters: Evidence from Mars and other planets. *Icarus*, 43, 1980.

[47] P. M. Schenk. Crater formation and modification on the icy satellites of Uranus and Saturn: Depth/diameter and central peak occurrence. *J. Geophys. Res.*, 94, 1989.

[48] C. R. Chapman and W. B. McKinnon. Cratering of planetary satellites. In J. A. Burns and M. S. Matthews, editors, *Satellies*. University of Arizona Press, Tucson, AZ, 1986.

[49] D. E. Smith, Maria T. Zuber, Roger J. Phillips, Sean C. Solomon, II Steven A. Hauck, Frank G. Lemoine, Erwan Mazarico, Gregory A. Neumann, Stanton J. Peale, Jean-Luc Margot, Catherine L. Johnson, Mark H. Torrence, Mark E. Perry, David D. Rowl ands, S ander Goossens, James W. Head, and Anthony H. Taylor. Gravity field and internal structure of Mercury from MESSENGER. *Science Report*, 2012.

[50] M. T. Zuber, D. E. Smith, A. F. Cheng, and T. D. Cole. The NEAR laser ranging investigation. *J. Geophys. Res.*, 102:23,761–23,773, 1997.

[51] K. K. Williams and M. T. Zuber. Measurement and analysis of lunar basin depths from Clementine altimetry. *Icarus*, 131:107–122, 1998.

[52] D. H. Baker, J. W. Head, C. I. Fassett, S. J. Kadish, D. E. Smith, M. T. Zuber, and G. A. Neumann. The transition from complex crater to peak-ring basin on the Moon: New observations from the Lunar Orbiter Laser Altimeter (LOLA) instrument. *Icarus*, 214:377–393, 2011.

[53] H. Hiesinger and J. W. Head III. New views of lunar geoscience: An introduction and overview. *Reviews in Mineralogy and Geochemistry*, 60, 2006.

[54] G. Salamunićcar, S. Lončarić, and E. Mazarico. LU60645GT and MA132843GT catalogues of lunar and martian impact craters developed using a crater shape-based interpolation crater detection algorithm for topography data. *Planet. and Space Sci.*, 60:236–247, 2012.